

HERMES: THE FAR-INFRARED EMISSION FROM DUST OBSCURED GALAXIES

J.A. CALANOG¹, J. WARDLOW¹, HAI FU¹, A. COORAY^{1,2}, R.J. ASSEF³, J. BOCK^{2,3}, C.M. CASEY⁴, A. CONLEY⁵,
D. FARRAH^{6,7}, E. IBAR⁸, J. KARTALTEPE⁹, G. MAGDIS¹⁰, L. MARCHETTI^{11,12}, S.J. OLIVER⁶, I. PÉREZ-FOURNON^{13,14},
D. RIECHERS², D. RIGOPOULOU^{15,10}, I.G. ROSEBOOM^{6,16}, B. SCHULZ^{2,17}, DOUGLAS SCOTT¹⁸, M. SYMEONIDIS¹⁹,
M. VACCARI^{12,20}, M. VIERO², M. ZEMCOV^{2,3}

Draft version April 18, 2013

ABSTRACT

Dust-obscured galaxies (DOGs) are a UV-faint, infrared-bright galaxy population that reside at $z \sim 2$ and are believed to be in a phase of dusty star-forming and AGN activity. We present far-infrared (far-IR) observations of a complete sample of DOGs in the 2 deg² of the Cosmic Evolution Survey (COSMOS). The 3077 DOGs have $\langle z \rangle = 1.9 \pm 0.3$ and are selected from 24 μm and r^+ observations using a color cut of $r^+ - [24] \geq 7.5$ (AB mag) and $S_{24} \geq 100 \mu\text{Jy}$. Based on the mid-IR spectral energy distributions, 47% are bump DOGs (star-formation dominated) and 10% are power-law DOGs (AGN-dominated). We use SPIRE far-IR photometry from the *Herschel* Extragalactic Multi-tiered Survey (HerMES) to calculate the IR luminosity and characteristic dust temperature for the 1572 (51%) DOGs that are detected at 250 μm ($\geq 3\sigma$). For the remaining 1505 (49%) that are undetected, we perform a median stacking analysis to probe fainter luminosities. Detected and undetected DOGs have average luminosities of $(2.8 \pm 0.4) \times 10^{12} L_{\odot}$ and $(0.77 \pm 0.08) \times 10^{12} L_{\odot}$, and dust temperatures of (34 ± 7) K and (31 ± 3) K, respectively. DOGs contribute 30% to the 24 μm -selected galaxies' infrared luminosity function, calculated using far-infrared observations. If the IR luminosity is extrapolated using the 24 μm flux density alone, it is overestimated by a factor of 2 on average. DOGs contribute 10 – 30% to the total star formation rate density of the Universe at $z = 1.5 - 2.5$, dominated by 250 μm detected and bump DOGs, compared to around 40% for all 24 μm galaxies above our flux limit. DOGs have a large scatter about the star-formation main sequence and their specific star-formation rates show that the observed phase of star-formation could be responsible for their observed stellar mass at $z \sim 2$.

Subject headings: Galaxies: luminosity function — Galaxies: star formation — Infrared: galaxies

1. INTRODUCTION

The bolometric luminosities of Luminous Infrared Galaxies (LIRGs; $L_{\text{IR}} \geq 10^{11} L_{\odot}$) and Ultra-LIRGs (ULIRGs; $L_{\text{IR}} \geq 10^{12} L_{\odot}$) are dominated by re-processed thermal dust emission, due to prodigious rates of star-formation activity, black hole accretion, or both. Locally, these sources are rare, although out to $z \sim 1$ they become more numerous and increasingly dominate the infrared luminosity function of galaxies with increasing redshift (Le Floc'h et al. 2005; Pérez-González et al. 2005; Caputi et al. 2007; Magnelli et al. 2009; Rodighiero et al. 2010; Eales et al. 2010). (U)LIRGs are thought to trace a phase of intense star-formation activity, which is likely followed by, or partially concurrent with, an episode of vigorous black hole accretion. Upon the cessation of these phases each produces an early-type galaxy (Genzel et al. 2001; Farrah et al. 2003; Lonsdale et al. 2006; Veilleux et al. 2009).

Studies using the Multiband Imaging Photometer for *Spitzer* (MIPS; Rieke et al. 2004) instrument onboard the *Spitzer Space Telescope* (Werner et al. 2004) have identified high-redshift ULIRGs from their 24 μm emis-

Canada

¹⁹ Mullard Space Science Laboratory, University College London, Holmbury St. Mary, Dorking, Surrey RH5 6NT, UK

²⁰ Astrophysics Group, Physics Department, University of the Western Cape, Private Bag X17, 7535, Bellville, Cape Town, South Africa

¹ Dept. of Physics & Astronomy, University of California, Irvine, CA 92697

² California Institute of Technology, 1200 E. California Blvd., Pasadena, CA 91125

³ Jet Propulsion Laboratory, 4800 Oak Grove Drive, Pasadena, CA 91109

⁴ Institute for Astronomy, University of Hawaii, 2680 Woodlawn Drive, Honolulu, HI 96822

⁵ Center for Astrophysics and Space Astronomy 389-UCB, University of Colorado, Boulder, CO 80309

⁶ Astronomy Centre, Dept. of Physics & Astronomy, University of Sussex, Brighton BN1 9QH, UK

⁷ Department of Physics, Virginia Tech, Blacksburg, VA 24061

⁸ Pontificia Universidad Católica de Chile, Departamento de Astronomía y Astrofísica, Vicuña Mackenna 4860, Casilla 306, Santiago 22, Chile

⁹ National Optical Astronomy Observatory, 950 North Cherry Avenue, Tucson, AZ 85719

¹⁰ Department of Astrophysics, Denys Wilkinson Building, University of Oxford, Keble Road, Oxford OX1 3RH, UK

¹¹ Department of Physical Sciences, The Open University, Milton Keynes MK7 6AA, UK

¹² Dipartimento di Fisica e Astronomia, Università di Padova, vicolo Osservatorio, 3, 35122 Padova, Italy

¹³ Instituto de Astrofísica de Canarias (IAC), E-38200 La Laguna, Tenerife, Spain

¹⁴ Departamento de Astrofísica, Universidad de La Laguna (ULL), E-38205 La Laguna, Tenerife, Spain

¹⁵ RAL Space, Rutherford Appleton Laboratory, Chilton, Didcot, Oxfordshire OX11 0QX, UK

¹⁶ Institute for Astronomy, University of Edinburgh, Royal Observatory, Blackford Hill, Edinburgh EH9 3HJ, UK

¹⁷ Infrared Processing and Analysis Center, MS 100-22, California Institute of Technology, JPL, Pasadena, CA 91125

¹⁸ Department of Physics & Astronomy, University of British Columbia, 6224 Agricultural Road, Vancouver, BC V6T 1Z1,

sion (Yan et al. 2004; Houck et al. 2005; Weedman et al. 2006; Fiore et al. 2008; Dey et al. 2008; Farrah et al. 2008; Fiore et al. 2009). Dey et al. (2008) exploited this technique in the Boötes field of the NOAO Deep Wide Field Survey (NDWFS) and presented a sample of dusty ULIRGs selected by the color cut $R - [24] \geq 14$ (Vega magnitudes; $S_{24}/S_R \geq 1000$). This color selection samples the rest-frame $7.7 \mu\text{m}$ polycyclic aromatic hydrocarbon (PAH) feature found in star-forming galaxies and causes the redshift distribution to have a biased average at $z \sim 2$. Also, at $z \sim 2$, the DOG selection falls within range of the power-law component of AGN emission in the mid-IR, which also identifies a population of active galactic nuclei (AGN). It is proposed that these dust-obscured galaxies (DOGs) are the latter stage of the sub-millimeter galaxy (SMGs; Hughes et al. 1998; Smail et al. 1997; Barger et al. 1998; Blain et al. 1999, among others) phase where an AGN is triggered while star formation is still occurring, causing some dust to be heated to higher temperatures (Dey et al. 2008) than in classic $850 \mu\text{m}$ selected SMGs. Pope et al. (2008) found that 30% of the SMGs are also DOGs, and of those SMG-DOGs, 30% are AGN-dominated ($\geq 50\%$ AGN contribution in mid-IR), consistent with this scenario. Using high resolution optical and near-IR (NIR) imaging from the *Hubble Space Telescope* to investigate DOG morphology, the studies of Bussmann et al. (2009) and Bussmann et al. (2011) found that the morphologies of bump (star-forming) DOGs, power-law (AGN dominated) DOGs, SMGs, and high redshift quiescent distant red galaxies (DRGs) are consistent with the picture that major merger-driven systems eventually all evolve into compact relaxed passive galaxies (Springel et al. 2005 and references therein). Furthermore, Narayanan et al. (2010) used N-body and hydrodynamic simulations to model the temporal evolution of high redshift galaxies and found that at the peak of the merger-driven galaxies' star formation rate, a galaxy can both be identified as an SMG and a DOG. The same study also found that during the stages after final coalescence, merger-driven DOGs transition from being star-formation dominated to being AGN dominated.

The launch of the *Herschel Space Observatory*²¹ (Pilbratt et al. 2010) enables the direct observation of DOGs in the far-IR regime, instead of extrapolating from spectral energy distribution (SED) templates or stacking (e.g. Dey et al. 2008; Pope et al. 2008). Melbourne et al. (2012) studied *Herschel*-detected DOGs with spectroscopic redshifts and showed that DOGs classified by their mid-IR SEDs as either bump (star-forming) or power-law (AGN-dominated) have $250 \mu\text{m}/24 \mu\text{m}$ flux-density ratios that are consistent with local ULIRGs of the respective classes. Penner et al. (2012) used *Herschel* data to show that DOGs' high rest-frame MIR/UV flux density ratios are due to varying amounts of UV dust obscuration, and speculated that it is caused by differing degrees of alignment between dust and stars, or simply by the differences in total dust content.

The focus of this paper is to extend the study of DOGs in the far-IR to a complete sample in order to extract statistical conclusions about this galaxy population. We generate our DOG catalog using Subaru r^+ band and MIPS $24 \mu\text{m}$ data from the Cosmological Evolution Survey (COSMOS; Scoville et al. 2007) and combine it with multi-wavelength data in the far-IR from the *Herschel* Multi-tiered Extragalactic Survey²² (HerMES; Oliver et al. 2012). We calculate IR luminosities, star formation rate (SFR) and dust temperatures for all DOGs detected at $250 \mu\text{m}$ and employ a stacking analysis to calculate the average properties of the undetected population and thus to probe fainter luminosities. For DOGs at $z = 1.5 - 2.5$, we generate a luminosity function and calculate the star-formation rate density at $z \sim 2$.

This paper is organized as follows. Section 2 describes the dataset and sample selection. The results and our analysis are presented in Section 3. We summarize our conclusions in Section 4. Unless specifically stated, all magnitudes are reported in the AB system, where $-2.5 \log_{10} S_\nu (\mu\text{Jy}) + 23.9 = \text{AB mag}$, and assume a standard ΛCDM cosmology with $H_0 = 70 \text{ km s}^{-1} \text{Mpc}^{-1}$, $\Omega_M = 0.3$, and $\Omega_\Lambda = 0.7$.

2. DATA AND SAMPLE SELECTION

2.1. Far-Infrared Data

The 250, 350, and $500 \mu\text{m}$ far-IR data were obtained using the *Herschel*-Spectral and Photometric Imaging Receiver (SPIRE; Griffin et al. 2010; Swinyard et al. 2010) as part of HerMES, with an area coverage that completely overlaps with the MIPS observations of the 2 deg^2 COSMOS field. We use the first data release (DR1) of HerMES maps that were processed using the *smap* pipeline (Levenson et al. 2010). The reduced maps reach 3σ point source depths of 8, 10, and 14 mJy, in the 250, 350, and $500 \mu\text{m}$ channels respectively, where σ is the combined instrumental and confusion noise. For sources with $S_{250} \geq 3\sigma$, we use the listed photometry from the HerMES cross-identification catalog (XID). This catalog uses known positions of $24 \mu\text{m}$ sources as a prior, and estimates SPIRE fluxes via linear inversion methods. Model selections are used to account for, and prevent overfitting, and to optimize the $24 \mu\text{m}$ input. The fitting method is outlined in more detail in Roseboom et al. (2010).

2.2. Optical and Mid-Infrared Data

We use deep Subaru Suprime-Cam (Komiyama et al. 2003) aperture-corrected r^+ photometry supplied by the COSMOS catalog (Capak et al. 2007). The 5σ point-source depth for a $3''$ aperture is 26.8 mag.

The mid-IR data are from *Spitzer* observations carried out by the COSMOS *Spitzer* Survey (S-COSMOS; Sanders et al. 2007) using the Infrared Array Camera (IRAC; Fazio et al. 2004) and MIPS. The IRAC 5σ depths at 3.6, 4.5, 5.6, and $8.0 \mu\text{m}$ for an aperture-corrected $1.9''$ aperture, are 0.50, 0.6, 3, and $5 \mu\text{Jy}$, respectively. The MIPS $24.0 \mu\text{m}$ 5σ point source depth is $55 \mu\text{Jy}$.

We next generate a MIPS $24 \mu\text{m}$ -selected catalog that

²¹ *Herschel* is an ESA space observatory with science instruments provided by European-led Principal Investigator consortia and with important participation from NASA.

²² <http://hermes.sussex.ac.uk/>

combines the Subaru and *Spitzer* datasets, using a two-step cross-matching process within the 2 deg^2 of the Subaru deep area in order to find optical counterparts for each source (Fu et al. 2010). Firstly, the $24 \mu\text{m}$ coordinates are matched to the closest IRAC detection within a $2''$ search radius, then the nearest optical counterpart is identified within $1''$ of the IRAC position. Finally, sources near bright stars that were within the Subaru/optical and *Spitzer*/IRAC $3.6 \mu\text{m}$ coverage were removed from the catalog to avoid contamination. The final catalog has 48,474 sources and is $\geq 90\%$ complete above $S_{24} = 80 \mu\text{Jy}$.

2.3. Sample Selection

DOGs are selected in the standard manner, by identifying sources with $r^+ - [24] \geq 7.5$ (AB mag; $S_{24}/S_{r^+} \geq 1000$) and we require $[24] \leq 18.90$ mag ($S_{24} \geq 100 \mu\text{Jy}$) due to the depth of the $24 \mu\text{m}$ data. Using these criteria 3077 of the 48474 (6%) COSMOS $24 \mu\text{m}$ sources are identified as DOGs (Fig. 1). The mid-IR SED of each DOG is examined using IRAC photometry ($\geq 5\sigma$) to classify whether a DOG contains a bump-like feature or resembles a power-law. For this study, a “bump” DOG is defined if it satisfies one of the following: $S_{3.6} \leq S_{4.5} \geq S_{8.0}$; $S_{4.5} \leq S_{5.8} \geq S_{8.0}$; or $S_{3.6} \leq S_{4.5} \geq S_{5.8}$. Here $S_{[3.6,4.5,5.8,8.0]}$ represent the flux densities in the 4 IRAC channels. Conversely, we label a DOG as “power-law” if it satisfies $S_{3.6} \leq S_{4.5} \leq S_{5.8} \leq S_{8.0}$. Previous studies have interpreted sources that feature a bump in the mid-IR SED to be the stellar continuum peak at rest-frame $1.6 \mu\text{m}$, tracing stellar emission and likely star-formation dominated (e.g. Yan et al. 2005; Sajina et al. 2007), while a power-law is dominated by AGN continuum emission (e.g. Weedman et al. 2006; Donley et al. 2007). Bump DOGs compose 47% of our sample, while power-law DOGs are rarer, totaling 10%. The remaining 43% are not classified due to one of two possibilities: insufficient or low signal to noise IRAC data; or an SED shape that does not satisfy the above criteria. For the latter case, most of the sources are at $z < 2$ (median of $z = 1.1$), such that the rest-frame $1.6 \mu\text{m}$ stellar continuum peak lies outside the wavelength range of the IRAC channels.

2.4. Redshifts

All redshifts used in this paper are from COSMOS. Spectroscopic redshifts are used when available (35 sources, 1%; Lilly et al. 2007, Kartaltepe et al., in prep), although virtually all of our DOG sample (2979 sources, 97%) use photometric redshifts. The photometric redshifts are derived from 30 photometric bands (Ilbert et al. 2009), providing $\sigma_{\Delta z/(1+z)} = 0.02$, for $24 \mu\text{m}$ sources that lie at $z = 1.5 - 3$ and have the same r^+ mag range as DOGs. The 61 DOGs that are X-ray detected use photometric redshifts that also account for AGN flux variability (Salvato et al. 2009). Also, two sources do not have a redshift estimate and are excluded from our sample. We note that the sharp peak in the redshift distribution at $z = 1.95$ is due to rounding from the redshift values associated with the bin size used and no spatial correlation is observed.

The redshift distribution of the final sample of 3075 DOGs is shown in Fig. 2, with a mean of $\langle z \rangle = 1.9 \pm 0.3$.

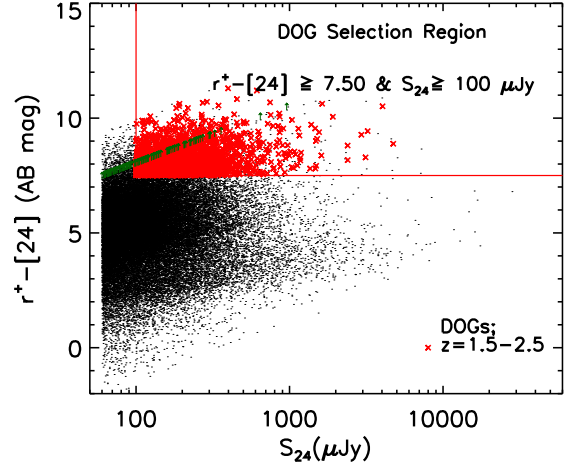


Figure 1. $r^+ - [24]$ as a function of $24 \mu\text{m}$ flux. DOGs are selected to have $r^+ - [24] \geq 7.5$ AB mag and $S_{24} \geq 100 \mu\text{Jy}$. DOGs with $z = 1.5 - 2.5$ are highlighted in red, while green arrows are lower limits for sources that were undetected in the r^+ -band. The 1901 DOGs at $z = 1.5 - 2.5$ are not biased in $r^+ - [24]$ when compared to other DOGs.

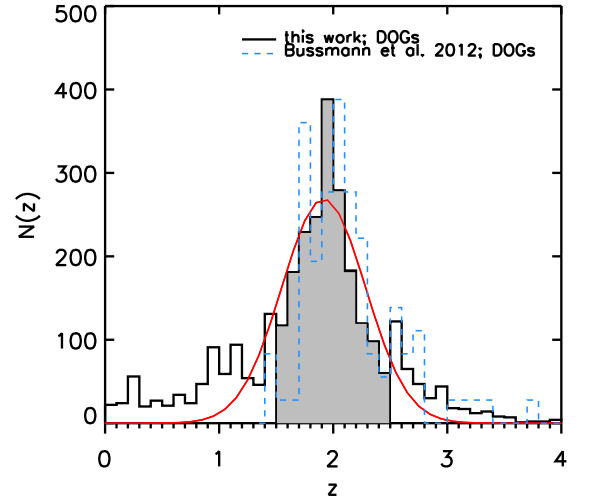


Figure 2. Photometric redshift distribution of DOGs in the COSMOS field. We show the DOG distribution from Bussmann et al. (2012) normalized to have equal peaks for comparison. The filled region highlights the range $z = 1.5 - 2.5$, considered for our analysis. We find $\langle z \rangle = 1.9 \pm 0.3$, assuming a Gaussian distribution, as shown in red.

The sample of 90 DOGs in the Boötes field with spectroscopic redshifts from Bussmann et al. (2012), normalized to have an equal peak with our sample, is also shown. The two samples have a consistent mean z of 1.9 ± 0.02 and 2.1 ± 0.5 , for our sample and the Bussmann et al. (2012) sample, respectively.

3. ANALYSES AND RESULTS

3.1. Far-Infrared Spectral Energy Distributions

Using the COSMOS redshifts and *Herschel* 250, 350 and $500 \mu\text{m}$ photometry, we fit the far-IR SED and calculate the rest-frame IR luminosity ($8 - 1000 \mu\text{m}$) and characteristic dust temperature. We divide the DOGs

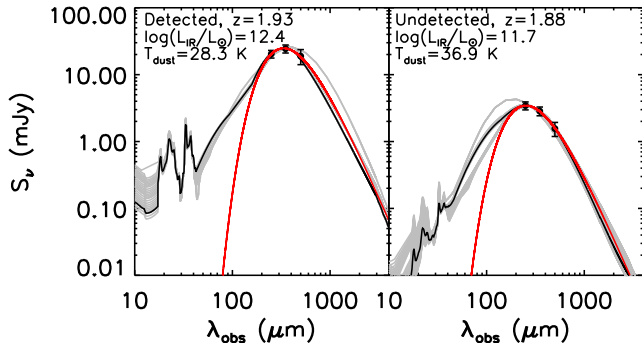


Figure 3. Example SED fitting for a detected DOG (*left panel*) and an undetected DOG (*right panel*). The black curve shows the best fitting template to the SPIRE data points (black circles) and the gray curves show CE01 templates that provide acceptable fits consistent with the error bars. The red curve shows the best fit modified blackbody, which we use to calculate the dust temperature.

into two subsamples based on $250\,\mu\text{m}$ detections: a DOG is considered *Herschel*-detected if it satisfies $S_{250} \geq 3\sigma_{250}$ (where σ_{250} is the total uncertainty due to the instrumental and confusion noise), and undetected otherwise. Of our DOG sample, 51% are thus *Herschel*-detected. To calculate the characteristic dust temperature, for each of these we use the available SPIRE flux densities to fit a modified blackbody of the form

$$S_\nu \propto B_\nu(T_{\text{dust}})\nu^\beta, \quad (1)$$

where ν is frequency, β is the dust emissivity, fixed to the typical value of 1.5 (Draine 2003), T_{dust} is the dust temperature and B_ν is the Planck function, defined as

$$B_\nu = \frac{2h\nu^3}{c^2} \frac{1}{e^{h\nu/k_B T_{\text{dust}}} - 1}. \quad (2)$$

Here h is Planck’s constant, c is speed of light, and k_B is Boltzmann’s constant. The temperature we calculate is insensitive to and consistent with the reported error bars from varying β slightly. All $250\,\mu\text{m}$ -detected DOGs are also detected in one other band can be fitted with this function.

We derive estimates of the IR luminosity by fitting the available SPIRE data to the SED template library of Chary & Elbaz (2001) (hereafter CE01). The template with the minimum χ^2 is chosen for the best fit. The uncertainty in IR luminosity is derived by first producing 1000 mock catalogs for each source that assume a Gaussian distribution centered around the listed SPIRE flux density, with a dispersion equal to the average SPIRE flux density error. The IR luminosity per source is recalculated 1000 times and the standard deviation of the IR luminosity distribution is the error in our calculation. Examples of the SED template and modified blackbody fitting are shown in Fig. 3.

The IR luminosity ($8 - 1000\,\mu\text{m}$) is converted to star formation rate using (Kennicutt 1998)

$$\text{SFR}(\text{M}_\odot \text{yr}^{-1}) = 1.72 \times 10^{-10} L_{\text{IR}}(L_\odot), \quad (3)$$

which assumes a Salpeter initial mass function (IMF). We note that in our study we assume that UV emission will provide negligible contribution to the total star formation rate, as validated by Penner et al. (2012).

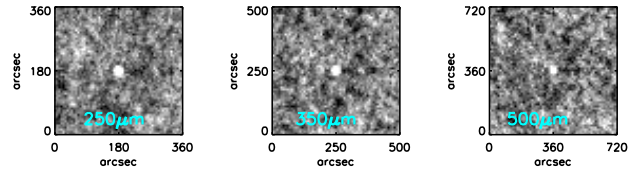


Figure 4. Example median stacking results of *Herschel*-undetected DOGs at 250, 350, and $500\,\mu\text{m}$ for undetected DOGs at $z = 1.75$ to 2.00

To measure the average flux density of the undetected DOGs, we bin the sources in redshift and for each bin stack on the SPIRE residual maps. These maps are generated by performing a blind extraction and PSF-subtraction to prevent contamination of individually detected sources. We use the publicly available IDL stacking library from Béthermin et al. (2010) to perform the stacking²³. Each stacked image was converted from the native Jy beam^{-1} to Jy pixel^{-1} and aperture photometry with an aperture size equal to $22''$, $30''$, and $42''$ for 250, 350 and $500\,\mu\text{m}$ respectively, is performed to calculate the flux of the stacked images. These aperture flux densities are consistent with those measured in the central pixel when the stacked map is in units of Jy beam^{-1} .

The observed stacked flux densities are corrected for the boosting from clustering bias by dividing by factors of 1.07, 1.10 and 1.20 at 250, 350 and $500\,\mu\text{m}$, respectively. The appropriate correction factors vary with clustering strength and are thus population dependent. These values were calculated by Béthermin et al. (2012) for $24\,\mu\text{m}$ sources and are valid for DOGs because the observed correlation lengths, r_0 (a proxy for clustering amplitude), for DOGs (Brodwin et al. 2008) and the parent population of $24\,\mu\text{m}$ sources (Magliocchetti et al. 2008; Starikova et al. 2012) are consistent. Errors in the photometry are calculated from bootstrapping the sources to be stacked. For each redshift bin, the clustering-corrected SPIRE flux densities of undetected DOGs are set to equal the median stacked flux densities and the IR luminosity and dust temperature are calculated using the same method as for the *Herschel*-detected DOGs. The (clustering-corrected) stacked fluxes and errors, and the resulting average infrared luminosities and dust temperatures are shown in Table 1.

We note that the stacks of $250\,\mu\text{m}$ images are on average a factor of 2 deeper than our 3σ detection limit. In Fig. 4 we show an example of the median stacked images for 250, 350 and $500\,\mu\text{m}$ from left to right at $z = 1.75 - 2.00$ and an example SED using stacked SPIRE flux densities for an undetected DOG at $z = 1.88$ is shown in the right panel of Fig. 3. Each image stack is large enough to provide a good estimate for the background noise.

Fig. 5 shows IR luminosities of the *Herschel*-detected DOGs as a function of redshift. The average IR luminosity for detected and undetected DOGs is $(2.8 \pm 0.3) \times 10^{12} L_\odot$ and $(6.0 \pm 1.0) \times 10^{11} L_\odot$, respectively. LIRGs

²³ The IDL library from Béthermin et al. (2010) is available at <http://www.ias.u-psud.fr/irgalaxies/downloads.php>

Table 1
SPIRE Stacking Results

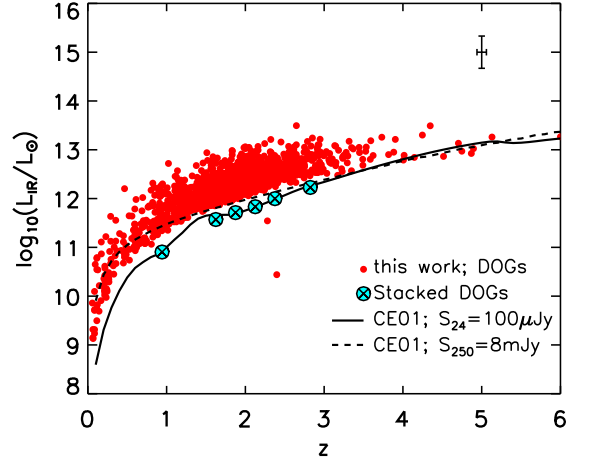
z	S_{250}^a (mJy)	S_{350}^a (mJy)	S_{500}^a (mJy)	N^b	L_{IR}^c ($\times 10^{12} L_{\odot}$)	T_{dust}^c (K)
< 1.50	4.2 ± 0.5	3.0 ± 0.4	2.1 ± 0.4	354	0.16 ± 0.13	25.1 ± 5.5
$1.50 - 1.75$	3.5 ± 0.5	2.6 ± 0.5	1.7 ± 0.4	218	0.37 ± 0.02	34.6 ± 0.9
$1.75 - 2.00$	3.4 ± 0.5	2.9 ± 0.4	1.6 ± 0.4	406	0.52 ± 0.07	37.2 ± 0.9
$2.00 - 2.25$	4.3 ± 0.6	3.9 ± 0.6	1.7 ± 0.5	237	0.68 ± 0.06	40.0 ± 1.0
$2.25 - 2.50$	4.3 ± 1.1	3.7 ± 0.9	2.7 ± 0.7	82	1.00 ± 0.21	37.8 ± 0.8
> 2.5	4.9 ± 0.7	4.0 ± 0.6	2.9 ± 0.6	185	1.71 ± 2.8	44.3 ± 6.3

Notes^a Listed flux densities are from median stacking. The errors are from bootstrapping.^b Number of sources per redshift bin.^c Average and standard deviation per bin.

($10^{11} \leq L_{\text{IR}}(L_{\odot}) \leq 10^{12}$) comprise 15% of *Herschel*-detected DOGs and 75% for *Herschel*-undetected DOGs. ULIRGs ($10^{12} \leq L_{\text{IR}}(L_{\odot}) \leq 10^{13}$) make up 78% of the *Herschel*-detected and 15% for *Herschel*-undetected DOGs. Hyper-luminous infrared galaxies (HLIRGs ($\geq 10^{13} L_{\odot}$)) are the rarest, totaling 2% for *Herschel*-detected DOGs and none for *Herschel*-undetected DOGs. Although we note that there is additional uncertainty in the fractional contributions of the undetected sources, due to the use of stacked average fluxes, which minimizes the contribution from extreme sources. *Herschel*-detected power-law, or AGN-dominated DOGs, have on average $L_{\text{IR}} = (4.5 \pm 0.5) \times 10^{12} L_{\odot}$, making them more IR-luminous than *Herschel*-detected bump, star-forming DOGs, which have $L_{\text{IR}} = (3.1 \pm 0.4) \times 10^{12} L_{\odot}$, which is consistent with the findings of Melbourne et al. (2012). Selection effects are investigated by calculating the IR luminosity of a representative CE01 template, scaled such that $S_{24} = 100 \mu\text{Jy}$ or $S_{250} = 8 \text{ mJy}$, as shown in Fig. 5. The local maxima in IR luminosity at $z \sim 1.5$ in the $24 \mu\text{m}$ curve is due to the rest-frame $9.7 \mu\text{m}$ silicate absorption feature. The lack of DOGs below the $24 \mu\text{m}$ and $250 \mu\text{m}$ limit at a given redshift leads us to conclude that the apparent trend in Fig. 5 that IR luminosity is increasing with redshift is a selection effect.

Figure 6 shows dust temperatures as a function of IR luminosities for DOGs, color-coded by redshift. The average characteristic dust temperature is $T_{\text{dust}} = (34 \pm 7) \text{ K}$ and $(37 \pm 5) \text{ K}$ for *Herschel*-detected and undetected DOGs, respectively. *Herschel*-detected power-law DOGs and bump DOGs have average $T_{\text{dust}} = (37 \pm 6) \text{ K}$ and $(35 \pm 7) \text{ K}$, respectively, and is consistent with each other. We consider sample selection effects in the $T_{\text{dust}} - L_{\text{IR}}$ plane by calculating IR luminosities and dust temperatures of the CE01 templates with $S_{250} = 8 \text{ mJy}$ and $S_{24} = 100 \mu\text{Jy}$. The $250 \mu\text{m}$ flux limit causes two selection effects: the first biases against hot sources, and the second is a lower luminosity limit that is redshift dependent (Fig. 6). This second effect causes an apparent trend that the warmest and IR luminous sources lie at high redshifts. The $24 \mu\text{m}$ flux limit produces a similar effect. We observe that the dearth of sources at high luminosities and low dust temperatures is not caused by selection bias and is a real effect. This is consistent with Symeonidis et al. (2013), who found that cold cirrus-dominated SEDs (Rowan-Robinson et al. 2010) are rare in the most IR luminous galaxies.

The results shown in Fig. 6 suggest that DOGs span a wider range of dust temperatures than $z \sim 2$ galaxy

**Figure 5.** IR luminosity as a function of redshift for *Herschel*-detected DOGs and the median IR luminosity for stacked DOGs. A representative template from Chary & Elbaz (2001) scaled to the DOG $24 \mu\text{m}$ (solid curve) and $250 \mu\text{m}$ detection limit (dashed curve) are also shown. A typical error bar is shown at the top right. The apparent trend that IR luminosity increases with redshift is a selection effect.**Table 2**
Average DOG IR Luminosities and Dust Temperatures

Type	L_{IR} ($\times 10^{12} L_{\odot}$)	T_{dust} (K)
Detected ^a	2.8 ± 0.3	33 ± 7
Undetected ^a	0.6 ± 0.1	37 ± 5
Bump*	4.5 ± 0.4	34 ± 7
Power-law*	3.1 ± 0.4	37 ± 6

Notes^a Detected sources satisfy: $S_{250} \geq 3\sigma$; undetected sources have $S_{250} < 3\sigma$.

* Power-law (AGN-dominated) and bump (star-forming) median IR luminosities are from the detected sample.

populations selected at longer wavelengths. While this may be true, it is more likely due to the different selection effects associated with each galaxy population. For example, SMGs (by which we mean $850 \mu\text{m}$ or 1 mm selected sources) are biased towards detecting cold-dust dominated sources because hot sources are missed by sub-mm surveys (Casey et al. 2009; Chapin et al. 2009). Optically-faint radio galaxies (OFRGs; Casey et al. 2009; Magnelli et al. 2010), which share similar stellar

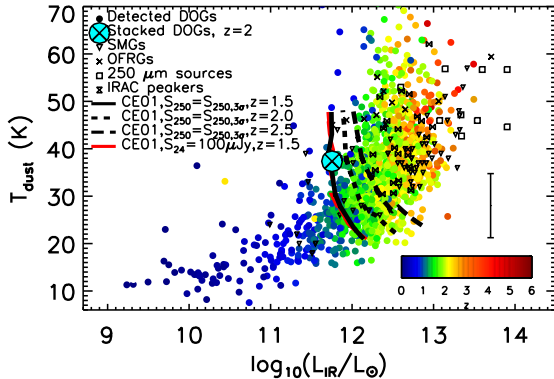


Figure 6. Dust temperatures and infrared luminosities for DOGs compared to other $z \sim 2$ galaxy populations (SMGs: Magnelli et al. 2012, OFRGs: Casey et al. 2009; Magnelli et al. 2010, $250 \mu\text{m}$ sources: Casey et al. 2011, IRAC peakers: Magdis et al. 2010). We show *Herschel*-detected DOGs, colored by redshift. The average IR luminosity and dust temperature of *Herschel*-undetected DOGs at $z = 2$ is represented by the solid cyan circle. The black curves represent the selection effects from estimating the dust temperature and IR luminosity by considering templates from Chary & Elbaz (2001) at $z = 1.5, 2.0$, and 2.5 , with $S_{250} = 8 \text{ mJy}$, our 3σ detection limit. The red curve is for $S_{24} = 100 \mu\text{Jy}$ at $z = 1.5$. We conclude that the apparent trend that hotter sources are at higher redshifts may be a selection effect and that the absence of sources with high luminosities and colder temperatures is not a selection effect.

masses, radio luminosities, and UV spectra as SMGs demonstrate this, while we also note that the radio-detection limit is biased against the coldest sources (e.g. Wardlow et al. 2011). DOGs are more insensitive to these selection biases and thus show a wider range of temperatures. Magdis et al. (2010) found similar results when investigating the characteristic dust temperatures for IRAC peakers at $z \sim 2$ and showed that mid-IR selected sources bridge the gap in temperature ranges between OFRGs and SMGs. We note that the $250 \mu\text{m}$ selected sources suffer from the same selection biases as our *Herschel*-detected DOGs but shifted to higher luminosities due to their shallower $250 \mu\text{m}$ detection limit.

3.2. Infrared Luminosity Function at $z \sim 2$

We compute the IR luminosity function of DOGs using the $1/V_{\text{max}}$ method (Schmidt 1978), defined as

$$\Phi(L)\Delta L = \sum_i \frac{1}{V_{\text{max},i}}, \quad (4)$$

where V_{max} is the maximum comoving volume of the i th source such that it would be detected and included in the sample. We consider the peak of the redshift distribution using only DOGs at $z = 1.5 - 2.5$. For the *Herschel*-detected DOGs we use two flux limits to determine V_{max} : $S_{24} = 100 \mu\text{Jy}$; and $S_{250} = 8 \text{ mJy}$. These are the two detection limits of the survey. For the *Herschel*-undetected sample, the $24 \mu\text{m}$ flux limit alone was used to calculate V_{max} . The uncertainties are from Poisson statistics and binning errors, where the binning errors are calculated by generating the IR luminosity function 1000 times from IR luminosities calculated from artificial SPIRE flux densities described in Section 3.1 and taking the standard deviation per IR luminosity bin. The

DOG IR luminosity function at $z \sim 2$ is presented in Fig. 7 and Table 3. The faint end of the IR luminosity function for *Herschel*-undetected and detected DOGs are coadded, which affects the lowest luminosity bin for *Herschel*-detected DOGs the most, showing a 0.20 dex increase.

For comparison, the DOG IR luminosity function for *Herschel*-detected DOGs and all DOGs, calculated by extrapolating the infrared luminosity from S_{24} using CE01 templates, is also shown in Fig. 7. The contribution to the number density of *Herschel*-detected DOGs relative to the whole DOG population is never 100% at each IR luminosity bin, which means that some IR luminosities of the undetected population are severely being overestimated. We find that the IR luminosities using this method are overestimated by a median factor of 1.8. This is consistent with the previous studies of $24 \mu\text{m}$ -selected galaxies at $z \sim 2$ (Houck et al. 2005; Yan et al. 2007; Daddi et al. 2007; Papovich et al. 2007; Pope et al. 2008; Elbaz et al. 2011) and stresses the importance of far-IR observations, further highlighting that the use of $24 \mu\text{m}$ flux density to estimate IR luminosity is problematic at $z > 1$, due to features from PAH emission, silicate absorption, and a power-law component from AGN.

We compare the number densities of DOGs to the parent population of sources with $S_{24} \geq 100 \mu\text{Jy}$ (Fig. 7). The luminosity function of $24 \mu\text{m}$ sources is calculated self-consistently using SPIRE data. There are 5932 sources in COSMOS with $S_{24} \geq 100 \mu\text{Jy}$ at $z = 1.5 - 2.5$, of which 32% are DOGs. Fig. 7 shows that DOGs have a smaller overall normalization in their luminosity function (since they are fewer in number) and their relative contribution to the $24 \mu\text{m}$ number density is roughly constant with increasing luminosity. Our results agree with the findings of Penner et al. (2012), where it was found that the distribution of IR luminosities for DOGs and the parent population of $24 \mu\text{m}$ sources are statistically indistinguishable.

Figure 7 also shows the $z = 1 - 3$ SMG luminosity function from Wardlow et al. (2011) from two redshift bins. DOGs are more common than SMGs at $z \sim 2$, which is reflected in the higher normalization in the luminosity function, although in the HLIRG regime, SMGs dominate. This is consistent with the picture that in order for DOGs to represent an evolutionary stage after the peak of star-formation rate in the SMG phase (Narayanan et al. 2010), they must have lower IR luminosities and star-formation rates. As is shown in fig. 8, the total star-formation rate density (ρ_{SFR}) provided by the two populations are approximately even despite the number and intensity of sources.

To calculate the contribution of DOGs to the ρ_{SFR} of the Universe at $z \sim 2$, we integrate the IR luminosity function and use equation 3. Figure 8 shows DOGs compared to other $z \sim 2$ galaxy populations. The total uncertainty in ρ_{SFR} is calculated from the quadrature sum of individual star-formation rate uncertainties and the standard deviation of ρ_{SFR} from the mock catalogs discussed in Section 3.1. Horizontal error bars represent the considered redshift interval. The value of ρ_{SFR} for DOGs at $z = 1.5 - 2.5$ is $(3.2 \pm 0.5) \times 10^{-2} \text{ M}_{\odot} \text{yr}^{-1} \text{Mpc}^{-3}$ which contributes to 12 – 29% of the overall ρ_{SFR} at $z = 2$ based on the models of Hopkins & Beacom (2006)

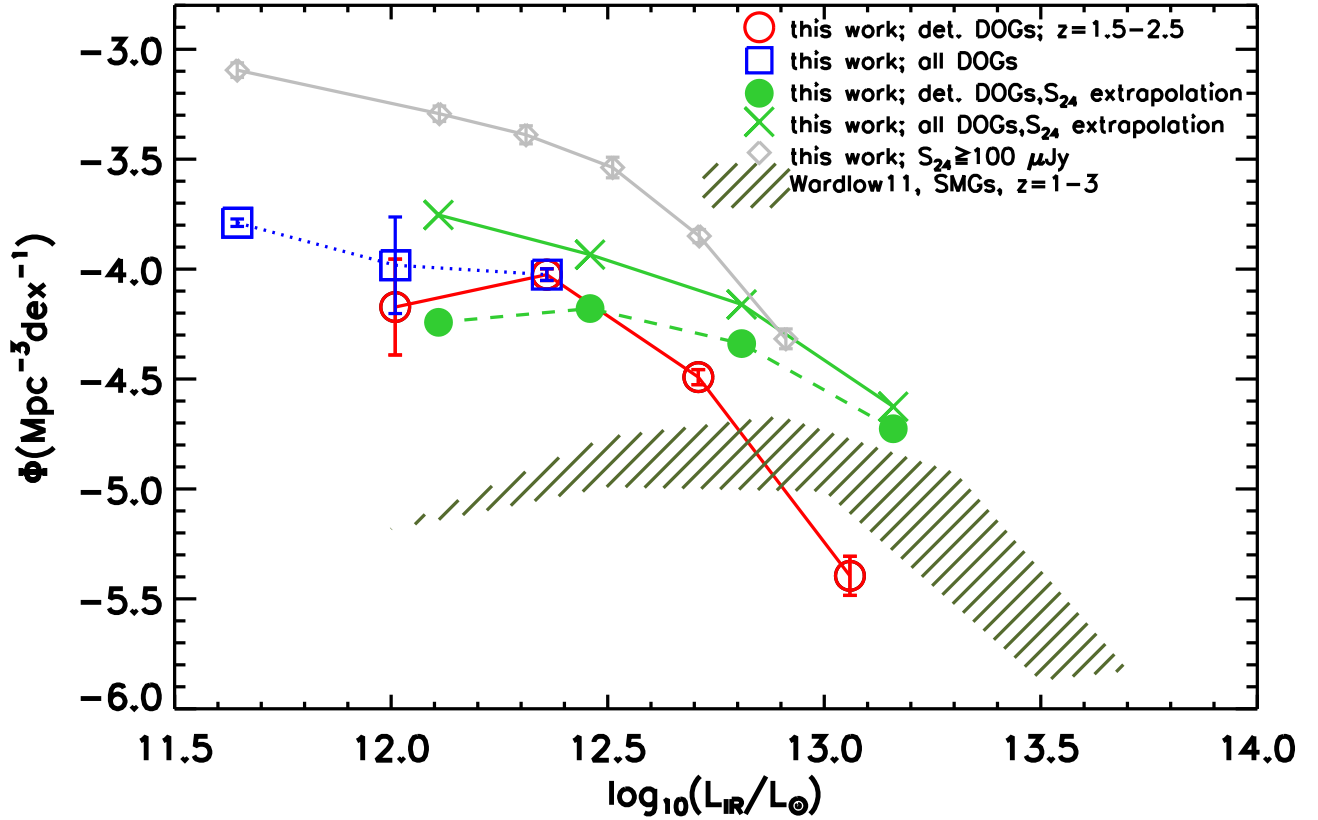


Figure 7. IR luminosity function of DOGs in the COSMOS field at $z \sim 2$. Individually *Herschel*-detected DOGs and the results from stacking undetected DOGs are shown. We compare this to an IR luminosity function for *Herschel*-detected DOGs and all DOGs generated from $24\mu\text{m}$ extrapolation using templates from Chary & Elbaz (2001), classical SMGs (Wardlow et al. 2011), and $24\mu\text{m}$ selected galaxies with $S_{24} \geq 100\mu\text{Jy}$. The results of stacking allow us to estimate the faint end of the LF and we note that using $24\mu\text{m}$ flux density to calculate IR luminosity results in overestimation. DOGs have a higher normalization, Φ^* , but a lower luminosity turnover, L^* , than SMGs.

Table 3
The IR Luminosity Function for DOGs at $z = 1.5 - 2.5$

$\log_{10}(L_{\text{IR}}/L_{\odot})$	Φ ($\text{Mpc}^{-3}\text{dex}^{-1}$)	N^a
11.40 – 11.80	$(-3.79 \pm 0.02)^b$	$(660)^b$
11.80 – 12.15	-4.17 ± 0.21 (-3.98 ± 0.22) ^b	150 (433) ^b
12.15 – 12.50	-4.03 ± 0.03 (-4.02 ± 0.09) ^b	522 (522) ^b
12.50 – 12.85	-4.49 ± 0.03	252
12.85 – 13.20	-5.40 ± 0.09	31

Notes

^a N is the number of sources per luminosity bin.

^b Numerical values in parenthesis include the stacked contribution.

and Burgarella et al. (2013). While 32% of the $24\mu\text{m}$ population at $z = 1.5 - 2.5$ are DOGs, their fractional contribution to the star-formation rate density is slightly larger because of their typically higher IR luminosities. When comparing against all $z = 1.5 - 2.5$ sources with $S_{24} \geq 100\mu\text{Jy}$, DOGs contribute 37% to the $24\mu\text{m}$ ρ_{SFR} . This is consistent with the relative distribution of DOGs' infrared luminosities compared against the $24\mu\text{m}$ population observed in the IR luminosity function.

The undetected and power-law sources provide non-dominant contributions to the total ρ_{SFR} of DOGs. The *Herschel*-undetected DOGs contribute 18% and power-law DOGs contribute just 9%. We note that even though

power-law DOGs are thought to be dominated by AGN emission in the IRAC bands, their far-IR emission is still likely dominated by star-formation (Elbaz et al. 2010). Indeed, even studies of the most active AGN have revealed that SED fits for *Herschel*-detected AGNs always required a starburst component in order to appear bright in the far-IR (Hatziminaoglou et al. 2010). As an attempt to quantify this claim, we use a simplified method to calculate an upper limit on the AGN contribution to the IR luminosity and star-formation rate in power-law DOGs and hence the contamination of ρ_{SFR} by AGN. We begin by scaling the AGN SEDs from Kirkpatrick et al. (2012) to the $24\mu\text{m}$ flux density of each power-law DOG and calculate the luminosity from the warm dust component. Then, by assuming that the warm dust component is entirely AGN-dominated and the cold dust component is entirely star-formation dominated, we can subtract the warm IR luminosity from the CE01 IR luminosity to calculate the residual contribution from star-formation. We find that power-law DOGs each have a maximum average contribution of 70% to the IR luminosity, which could contaminate ρ_{SFR} by $\sim 0.2 \times 10^{-2} \text{ M}_{\odot}\text{yr}^{-1}\text{Mpc}^{-3}$, which is only 6% of the total DOG ρ_{SFR} . In addition, we also estimate the dispersion of AGN contribution by normalizing quasar SED templates from Elvis et al. (1994), Richards et al. (2006), Polletta et al. (2007) and

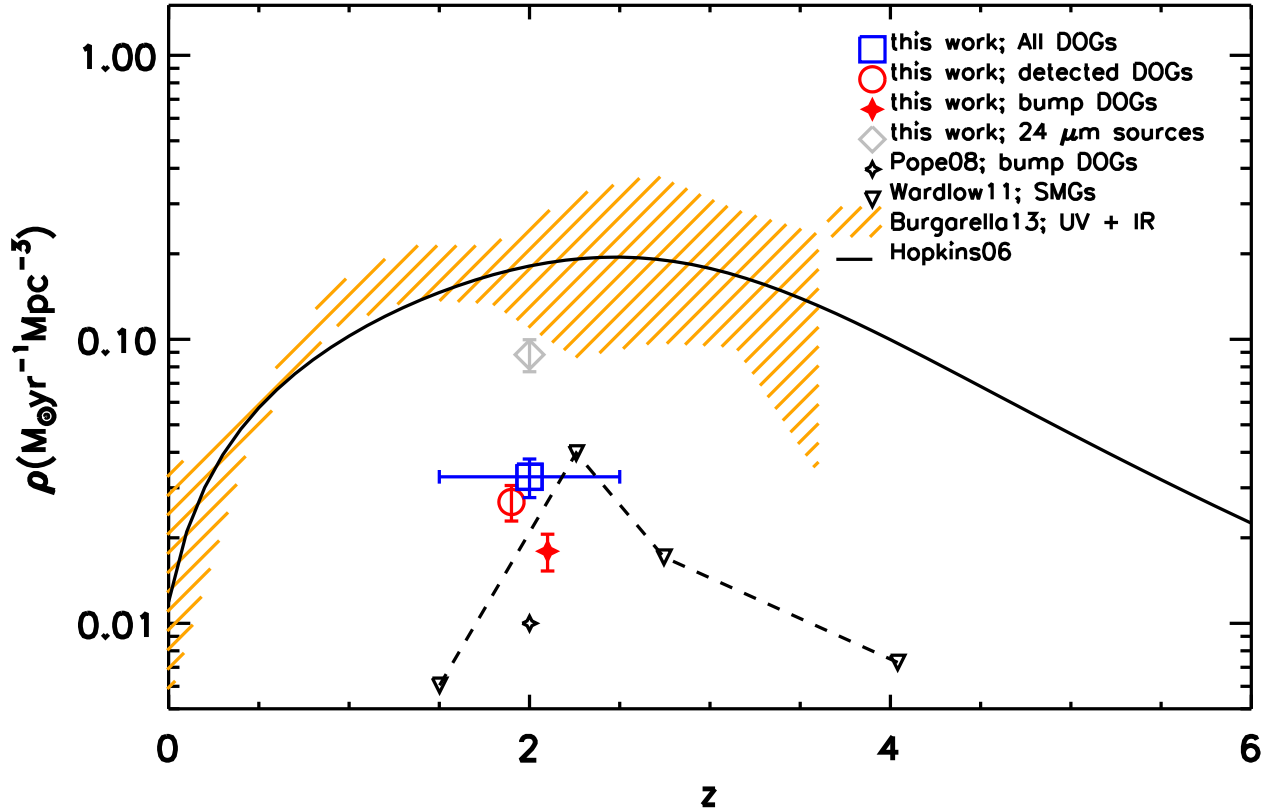


Figure 8. Star formation rate density (ρ_{SFR}) of all DOGs, *Herschel*-detected DOGs (offset by $z = -0.1$, for clarity), bump DOGs (offset by $z = +0.1$, for clarity) and all $S_{24} \geq 100 \mu\text{Jy}$ sources in COSMOS at $z = 1.5 - 2.5$. We also show ρ_{SFR} for bump DOGs ($S_{24} \geq 100 \mu\text{Jy}$) at $z = 2$ in the GOODS field from Pope et al. (2008) and SMGs from Wardlow et al. (2011). The evolution of ρ_{SFR} as a function of redshift from Hopkins & Beacom (2006) and Burgarella et al. (2013) are also shown. Based on these models, DOGs contribute 12 – 29% to the total ρ_{SFR} of the Universe at $z \sim 2$.

Dai et al. (2012) to the average power-law DOG $24 \mu\text{m}$ flux density at $z = 1.5 - 2.5$ and assume that the SEDs have no emission associated with star-formation. Under this assumption, the average AGN contributions to the individual galaxies’ IR luminosities range from 5% to 65%, depending on the SED, which corresponds to 0.005% to 6% contribution to the total DOG ρ_{SFR} .

We note that Pope et al. (2008) also examined bump (star-forming) DOGs at $z \sim 2$ and they calculated $\rho_{\text{SFR}} \sim 1 \times 10^{-2} \text{ M}_{\odot} \text{ yr}^{-1} \text{ Mpc}^{-3}$. This value is lower than the bump $\rho_{\text{SFR}} = 1.9 \pm 0.3 \times 10^{-2} \text{ M}_{\odot} \text{ yr}^{-1} \text{ Mpc}^{-3}$ that we measure. However, it is difficult to determine whether these two values are significantly different because Pope et al. (2008) do not provide an error on their measurement. We use their reported fractional error on the average IR luminosity ($1.1 \pm 0.7 \times 10^{12}$) to estimate that the minimum error on their ρ_{SFR} is $\sim 0.6 \times 10^{-2} \text{ M}_{\odot} \text{ yr}^{-1} \text{ Mpc}^{-3}$, in addition to the contribution from the counting error from their 62 sources (compared to our 1137 bump sources at $z = 1.5 - 2.5$). We also note that the selection criteria for the two studies are slightly different and if we were to use the Pope et al. (2008), we would identify 100 fewer bump DOGs (9% of bump DOGs are at $z = 1.5 - 2.5$). Therefore, we conclude that the two results are consistent, with our measurement providing a more accurate determination.

3.3. Stellar Mass Build-up

Using the stellar masses derived in Ilbert et al. (2010) (corrected to assume a Salpeter IMF by adding +0.24 dex), and our derived star-formation rates using *Herschel* data, we investigate where DOGs lie in the star-formation rate – stellar mass (SFR – M_*) plane. Disk galaxies with a steady star-formation mode are observed to form a tight correlation in their star-formation rates as a function of stellar mass, defining a “main sequence” (Daddi et al. 2007; Elbaz et al. 2011). Outliers in this relation are thought to be merger-driven starburst galaxies (Rodighiero et al. 2011 and references therein). In the top panel of Fig. 9 we show the star-formation rates and stellar masses for *Herschel*-detected DOGs, considering only those at $z = 1.5 - 2.5$ to minimize the effects of redshift evolution. Average error bars are plotted for star-formation rates and the uncertainties in stellar mass are fixed to 0.5 dex, which covers the systematic offset range due to the choice of extinction laws and stellar population synthesis models.

Fig. 9 shows that power-law DOGs and bump DOGs cover the same ranges in stellar mass and star-formation rate in the SFR – M_* plane, as expected if the far-IR is star-formation dominated. Our findings are also consistent with previous studies that investigated the similarities in properties of far-IR SEDs of *Herschel*-selected

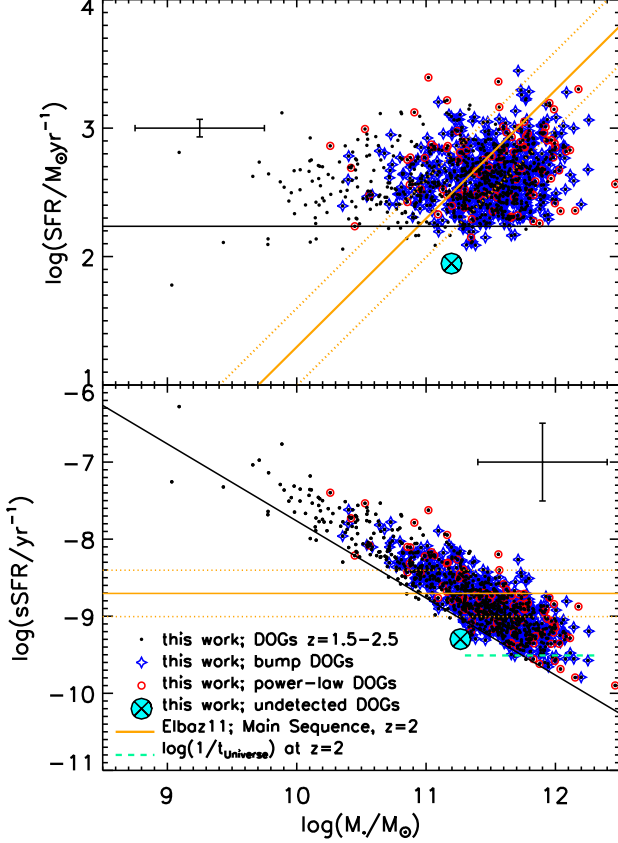


Figure 9. Star-formation rate (SFR; *top panel*) and specific star-formation rate (sSFR; *bottom panel*) as a function of stellar mass for DOGs at $z = 1.5 - 2.5$. Power-law DOGs and bump DOGs are statistically indistinguishable in the SFR– M_* plane. The sSFR at $z = 2$ using the relation for star-forming galaxies from Elbaz et al. (2011) and its conversion to SFR for the displayed range of masses is shown as the thick solid orange line in both panels. The orange dotted lines represent a factor of two dispersion from the derived SFR and sSFR. DOGs have a large scatter about the main sequence relation, having sources in the starburst, main sequence, and passive galaxy regimes. The thin horizontal black line in the top panel represents a minimum detectable star-formation rate at $z \sim 2$, caused by the $24\ \mu\text{m}$ flux density limit. Converting this to an sSFR value results in the diagonal line in the bottom panel, leading us to conclude that the apparent negative correlation between sSFR and stellar mass is a selection effect.

star-forming galaxies and AGN (Mullaney et al. 2012).

The infrared main sequence from Elbaz et al. (2011) for *Herschel*-selected star-forming galaxies at $z = 2$ is also shown in Fig. 9. DOGs have a significant amount of scatter about this relation, with 46% within a factor of 2 of the main-sequence, 24% above it and consistent with starbursts, and 31% below it in the more quiescent regime.

The bottom panel of Fig. 9 shows the specific star-formation rate ($\text{sSFR} = \frac{\text{SFR}}{M_*}$) as a function of stellar mass. The sSFR quantity measures the efficiency of star-formation, with its inverse giving a characteristic time-scale for the current burst length of star-formation activity. An apparent negative correlation in which lower mass DOGs exhibit higher sSFRs than their higher mass counterparts is observed for DOGs at $z = 2$, however this is largely a selection effect due to the flux limit of our sample. On the top panel of Fig. 9 we use the mini-

mum IR luminosity at $z = 2$ from our sample to represent a minimum detectable star-formation rate limit, shown as the horizontal line. We convert this to an sSFR value for a range of masses and this is shown as the diagonal line in the bottom panel. The logarithmic inverse age of the Universe in Gyr at $z = 2$ is ≈ -9.5 (dashed line in Fig. 9) and most DOGs have sSFRs larger than this, indicating that the observed phase of star-formation could be responsible for their observed stellar mass.

Finally, we use the known redshift distribution and the sSFRs of DOGs to compare their volume densities to their likely progenitors, SMGs. We estimate that the volume density of observed DOGs at $z = 1.5 - 2.5$ is $8 \times 10^{-5}\ \text{Mpc}^{-3}$. Using the median DOG sSFR to assume a characteristic lifetime of the DOG phase to be $\sim 1\ \text{Gyr}$, we can correct this density for the burst duty cycle to derive a volume density for the progenitors to be $\sim 1 \times 10^{-4}\ \text{Mpc}^{-3}$. This is consistent to the SMG volume density derived from Wardlow et al. (2011) at $z = 1.5 - 3$, which assumes the lifetime of the SMG phase to be 100 Myr, 10 times shorter than for DOGs. In this scenario, DOGs would have the same descendants as $z \sim 2$ SMGs, which, as discussed in Wardlow et al. (2011) and Hickox et al. (2012), are likely to be 2–3 L^* early-type galaxies.

4. CONCLUSIONS

We use *Herschel* HerMES data in COSMOS to study the far-IR emission from DOGs. The main findings are:

1. Out of 3077 DOGs, 51% are detected in *Herschel* ($S_{250} \geq 3\sigma = 8\ \text{mJy}$). We use stacking to probe the remaining undetected population and the stacked S_{250} is on average a factor of ~ 1.5 fainter than the individual detection limit.
2. The IR luminosity function of DOGs at $z = 1.5 - 2.5$ is calculated and shows that they contribute 30% to the luminosity function of $24\ \mu\text{m}$ -selected galaxies. The stacked infrared luminosities provide significant contribution in the lowest detected IR luminosity bin, causing an increase of ~ 0.2 dex. IR luminosities derived from extrapolating $24\ \mu\text{m}$ flux densities of local galaxy templates are over-estimated by a factor of around 2 and therefore, direct observations in the far-IR that sample the cold-dust emission from galaxies should always be used, if available, to calculate more accurate estimates.
3. DOGs contribute 10 – 30% to the overall star-formation rate density of the Universe and 39% for all $24\ \mu\text{m}$ galaxies with $S_{24} \geq 100\ \mu\text{Jy}$. We also note that when compared to the total DOG ρ_{SFR} , power-law (AGN dominated) DOGs provide minor contributions. The ρ_{SFR} for DOGs and SMGs are comparable at $z \sim 2$, however we note that DOGs are more numerous, with individually lower star-formation rates for DOGs than SMGs.
4. DOGs have a large scatter in the SFR – M_* plane, having sources in the starburst, main sequence and more quiescent galaxy regimes. The observed phase of star-formation for most DOGs is likely responsible for their observed stellar mass.

We thank Jason Melbourne for all his help and insightful discussions.

SPIRE has been developed by a consortium of institutes led by Cardiff Univ. (UK) and including: Univ. Lethbridge (Canada); NAOC (China); CEA, LAM (France); IFSI, Univ. Padua (Italy); IAC (Spain); Stockholm Observatory (Sweden); Imperial College London, RAL, UCL-MSSL, UKATC, Univ. Sussex (UK); and Caltech, JPL, NHSC, Univ. Colorado (USA). This development has been supported by national funding agencies: CSA (Canada); NAOC (China); CEA, CNES, CNRS (France); ASI (Italy); MCINN (Spain); SNSB (Sweden); STFC, UKSA (UK); and NASA (USA).

This research has made use of data from the HerMES project (<http://hermes.sussex.ac.uk/>). HerMES is a Herschel Key Programme utilizing Guaranteed Time from the SPIRE instrument team, ESAC scientists and a mission scientist. The data presented in this paper will be released through the HerMES Database in Marseille, HeDaM (<http://hedam.oamp.fr/HerMES/>).

We are thankful to the COSMOS collaboration for granting us access to their catalogs; and we gratefully acknowledge the contributions of the entire COSMOS team that have made this work possible. More information on the COSMOS survey is available at <http://hermes.sussex.ac.uk/>. This work is based (in part) on observations made with the *Spitzer Space Telescope*, which is operated by the Jet Propulsion Laboratory, California Institute of Technology under a contract with NASA. We acknowledge support from a GAANN fellowship (to JAC), NSF CAREER AST-0645427 (AC an HF) and NASA funds to the US HerMES team through JPL. S.O. acknowledges support from the Science and Technology Facilities Council [grant number ST/I000976/1].

Some of the data (spectroscopic redshifts) presented here were obtained at the W.M. Keck Observatory, which is operated as a scientific partnership among the California Institute of Technology, the University of California and the National Aeronautics and Space Administration. The Observatory was made possible by the generous financial support of the W.M. Keck Foundation. The authors wish to recognize and acknowledge the very significant cultural role and reverence that the summit of Mauna Kea has always had within the indigenous Hawaiian community. We are most fortunate to have the opportunity to conduct observations from this mountain.

Facilities: *Herschel* (SPIRE), *Spitzer* (IRAC, MIPS), Subaru (Suprime Cam), Keck

REFERENCES

- Barger, A. J., Cowie, L. L., Sanders, D. B., Fulton, E., Taniguchi, Y., Sato, Y., Kawara, K., & Okuda, H. 1998, *Nature*, 394, 248
- Béthermin, M., Dole, H., Beelen, A., & Aussel, H. 2010, *A&A*, 512, A78
- Béthermin, M., et al. 2012, *A&A*, 542, A58
- Blain, A. W., Kneib, J.-P., Ivison, R. J., & Smail, I. 1999, *ApJ*, 512, L87
- Brodwin, M., et al. 2008, *ApJ*, 687, L65
- Burgarella, D., et al. 2013, *A&A*, submitted
- Bussmann, R. S., et al. 2012, *ApJ*, 744, 150
- . 2009, *ApJ*, 693, 750
- . 2011, *ApJ*, 733, 21
- Capak, P., et al. 2007, *ApJS*, 172, 99
- Caputi, K. I., et al. 2007, *ApJ*, 660, 97
- Casey, C. M., et al. 2009, *MNRAS*, 399, 121
- Casey, C. M., Chapman, S. C., Smail, I., Alaghband-Zadeh, S., Bothwell, M. S., & Swinbank, A. M. 2011, *MNRAS*, 411, 2739
- Chapin, E. L., et al. 2009, *MNRAS*, 398, 1793
- Chary, R., & Elbaz, D. 2001, *ApJ*, 556, 562
- Daddi, E., et al. 2007, *ApJ*, 670, 156
- Dai, Y. S., et al. 2012, *ApJ*, 753, 33
- Dey, A., et al. 2008, *ApJ*, 677, 943
- Donley, J. L., Rieke, G. H., Pérez-González, P. G., Rigby, J. R., & Alonso-Herrero, A. 2007, *ApJ*, 660, 167
- Draine, B. T. 2003, *ARA&A*, 41, 241
- Eales, S. A., et al. 2010, *A&A*, 518, L23
- Elbaz, D., et al. 2011, *A&A*, 533, A119
- . 2010, *A&A*, 518, L29
- Elvis, M., et al. 1994, *ApJS*, 95, 1
- Farrah, D., Afonso, J., Efstathiou, A., Rowan-Robinson, M., Fox, M., & Clements, D. 2003, *MNRAS*, 343, 585
- Farrah, D., et al. 2008, *ApJ*, 677, 957
- Fazio, G. G., et al. 2004, *ApJS*, 154, 10
- Fiore, F., et al. 2008, *ApJ*, 672, 94
- . 2009, *ApJ*, 693, 447
- Fu, H., et al. 2010, *ApJ*, 722, 653
- Genzel, R., Tacconi, L. J., Rigopoulou, D., Lutz, D., & Tecza, M. 2001, *ApJ*, 563, 527
- Griffin, M. J., et al. 2010, *A&A*, 518, L3
- Hatziminaoglou, E., et al. 2010, *A&A*, 518, L33
- Hickox, R. C., et al. 2012, *MNRAS*, 421, 284
- Hopkins, A. M., & Beacom, J. F. 2006, *ApJ*, 651, 142
- Houck, J. R., et al. 2005, *ApJ*, 622, L105
- Hughes, D. H., et al. 1998, *Nature*, 394, 241
- Ilbert, O., et al. 2009, *ApJ*, 690, 1236
- . 2010, *ApJ*, 709, 644
- Kennicutt, Jr., R. C. 1998, *ApJ*, 498, 541
- Kirkpatrick, A., et al. 2012, *ApJ*, 759, 139
- Komiyama, Y., et al. 2003, in *Society of Photo-Optical Instrumentation Engineers (SPIE) Conference Series*, Vol. 4841, Society of Photo-Optical Instrumentation Engineers (SPIE) Conference Series, ed. M. Iye & A. F. M. Moorwood, 152–159
- Le Floc'h, E., et al. 2005, *ApJ*, 632, 169
- Levenson, L., et al. 2010, *MNRAS*, 409, 83
- Lilly, S. J., et al. 2007, *ApJS*, 172, 70
- Lonsdale, C. J., Farrah, D., & Smith, H. E. 2006, *Ultraluminous Infrared Galaxies*, ed. J. W. Mason, 285
- Magdis, G. E., et al. 2010, *MNRAS*, 409, 22
- Magliocchetti, M., et al. 2008, *MNRAS*, 383, 1131
- Magnelli, B., Elbaz, D., Chary, R. R., Dickinson, M., Le Borgne, D., Frayer, D. T., & Willmer, C. N. A. 2009, *A&A*, 496, 57
- Magnelli, B., et al. 2010, *A&A*, 518, L28
- . 2012, *A&A*, 539, A155
- Melbourne, J., et al. 2012, *AJ*, 143, 125
- Mullaney, J. R., et al. 2012, *MNRAS*, 419, 95
- Narayanan, D., et al. 2010, *MNRAS*, 407, 1701
- Oliver, S. J., et al. 2012, *MNRAS*, 424, 1614
- Papovich, C., et al. 2007, *ApJ*, 668, 45
- Penner, K., et al. 2012, *ApJ*, 759, 28
- Pérez-González, P. G., et al. 2005, *ApJ*, 630, 82
- Pilbratt, G. L., et al. 2010, *A&A*, 518, L1
- Polletta, M., et al. 2007, *ApJ*, 663, 81
- Pope, A., et al. 2008, *ApJ*, 689, 127
- Richards, G. T., et al. 2006, *ApJS*, 166, 470
- Rieke, G. H., et al. 2004, *ApJS*, 154, 25
- Rodighiero, G., et al. 2010, *A&A*, 518, L25
- . 2011, *ApJ*, 739, L40
- Roseboom, I. G., et al. 2010, *MNRAS*, 409, 48
- Rowan-Robinson, M., et al. 2010, *MNRAS*, 409, 2
- Sajina, A., Yan, L., Armus, L., Choi, P., Fadda, D., Helou, G., & Spoon, H. 2007, *ApJ*, 664, 713
- Salvato, M., et al. 2009, *ApJ*, 690, 1250
- Sanders, D. B., et al. 2007, *ApJS*, 172, 86
- Schmidt, K.-H. 1978, *Astronomische Nachrichten*, 299, 193
- Scoville, N., et al. 2007, *ApJS*, 172, 1
- Smail, I., Ivison, R. J., & Blain, A. W. 1997, *ApJ*, 490, L5
- Springel, V., Di Matteo, T., & Hernquist, L. 2005, *ApJ*, 620, L79
- Starikova, S., Berta, S., Franceschini, A., Marchetti, L., Rodighiero, G., Vaccari, M., & Vikhlinin, A. 2012, *ApJ*, 751, 126
- Swinyard, B. M., et al. 2010, *A&A*, 518, L4

- Symeonidis, M., et al. 2013, ArXiv e-prints
Veilleux, S., et al. 2009, ApJS, 182, 628
Wardlow, J. L., et al. 2011, MNRAS, 415, 1479
Weedman, D. W., Le Floch, E., Higdon, S. J. U., Higdon, J. L.,
& Houck, J. R. 2006, ApJ, 638, 613
Werner, M. W., et al. 2004, ApJS, 154, 1
Yan, L., et al. 2005, ApJ, 628, 604
—. 2004, ApJS, 154, 75
—. 2007, ApJ, 658, 778